

# Online Research @ Cardiff

This is an Open Access document downloaded from ORCA, Cardiff University's institutional repository: <https://orca.cardiff.ac.uk/id/eprint/119176/>

This is the author's version of a work that was submitted to / accepted for publication.

Citation for final published version:

Pegg, James T., Shields, Ashley E., Storr, Mark T., Scanlon, David O. and De Leeuw, Nora H. ORCID: <https://orcid.org/0000-0002-8271-0545> 2019.  
Noncollinear relativistic DFT + U calculations of actinide dioxide surfaces.  
Journal of Physical Chemistry C 123 (1) , pp. 356-366.  
10.1021/acs.jpcc.8b07823 file

Publishers page: <http://dx.doi.org/10.1021/acs.jpcc.8b07823>  
<<http://dx.doi.org/10.1021/acs.jpcc.8b07823>>

Please note:

Changes made as a result of publishing processes such as copy-editing, formatting and page numbers may not be reflected in this version. For the definitive version of this publication, please refer to the published source. You are advised to consult the publisher's version if you wish to cite this paper.

This version is being made available in accordance with publisher policies.  
See

<http://orca.cf.ac.uk/policies.html> for usage policies. Copyright and moral rights for publications made available in ORCA are retained by the copyright holders.



# Noncollinear Relativistic DFT + U Calculations of Actinide Dioxide Surfaces

James T. Pegg,<sup>\*,†,‡,§</sup> Ashley E. Shields,<sup>§</sup> Mark T. Storr,<sup>‡</sup> David O. Scanlon,<sup>†,||,⊥,¶</sup> and Nora H. de Leeuw<sup>†,#,⊥</sup>

<sup>†</sup>Department of Chemistry, University College London, 20 Gordon Street, London WC1H 0AJ, U.K.

<sup>‡</sup>Atomic Weapons Establishment (AWE) Plc, Aldermaston, Reading RG7 4PR, U.K.

<sup>§</sup>Oak Ridge National Laboratory, One Bethel Valley Road, Oak Ridge, Tennessee 37831, United States

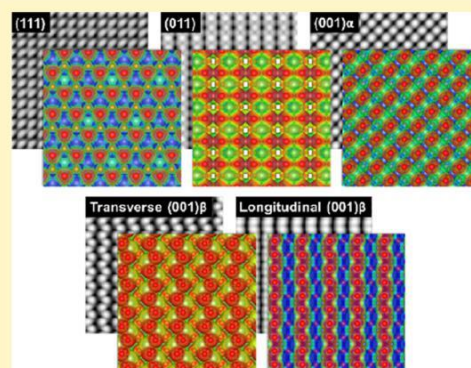
<sup>||</sup>Diamond Light Source Ltd., Diamond House, Harwell Science and Innovation Campus, Didcot, Oxfordshire OX11 0DE, U.K.

<sup>⊥</sup>Thomas Young Centre, University College London, Gower Street, London WC1E 6BT, U.K.

<sup>#</sup>School of Chemistry, Cardiff University, Main Building, Park Place, Cardiff CF10 3AT, U.K.

\* Supporting Information

**ABSTRACT:** A noncollinear relativistic PBEsol + U study of low-index actinide dioxides ( $\text{AnO}_2$ ,  $\text{An} = \text{U}$ ,  $\text{Np}$ , or  $\text{Pu}$ ) surfaces has been conducted. The importance of magnetic vector reorientation relative to the plane of the surface is highlighted; this has often been ignored in collinear nonrelativistic models. The use of noncollinear relativistic methods is key to the design of reliable computational models. The ionic relaxation of each surface is shown to be confined to the first three monolayers, and we have explored the configurations of the terminal oxygen ions on the reconstructed (001) surface. The reconstructed (001) surfaces are ordered as  $(001)\alpha\beta < (001)\alpha < (001)\beta$  in terms of energetics. Electrostatic potential isosurface and scanning tunneling microscopy images have also been calculated. By considering the energetics of the low-index  $\text{AnO}_2$  surfaces, an octahedral Wulff crystal morphology has been calculated.



## 1. INTRODUCTION

The surface chemistry of actinide dioxides ( $\text{AnO}_2$ ,  $\text{An} = \text{U}$ ,  $\text{Np}$ , or  $\text{Pu}$ ) is key to understanding corrosion mechanisms,<sup>1–8</sup> which impacts the design of long-term storage facilities and the industrial reprocessing of nuclear fuels.<sup>9–15</sup> The inexorable oxidation of actinide metal forms an oxide surface layer; where, the composition controls successive corrosion rates.<sup>1–5,7,16</sup> The rapid onset of corrosion results in: thermal excursions, the failure of containment vessels, and the resulting dispersal of nuclear materials. To reduce the risk of nuclear proliferation and assist in nuclear decommissioning, controlled oxidation of actinide metals offers a means of converting classified nuclear material to simple ingots.<sup>7</sup> In terms of fuel fabrication, the surface energetics also impact: fuel sintering behavior and particle morphology.<sup>17</sup>

As a result of the inhomogeneous and radioactive nature of An elements, few  $\text{AnO}_2$  experimental surface studies have been completed.<sup>9,13,18–24</sup> To compensate for experimental issues, computational methods offer another mode of study; although, a computational investigation of heavy-fermion systems is also challenging. To investigate the complex electronic structure by computational methods, one must consider exchange–correlation influences, relativistic contributions, and noncollinear magnetic behavior.<sup>25</sup> Only a limited number of studies have considered relativistic contributions (spin–orbit interaction,

SOI), which is important in the treatment of actinide systems.<sup>26–28</sup> In addition, the actinides often have complex (noncollinear) magnetic structures, and thus far no investigation of  $\text{AnO}_2$  surfaces has incorporated noncollinear magnetic behavior.<sup>27,29</sup>

The actinides are highly correlated f-electron systems for which conventional density functional theory (DFT) methods calculate an incorrect electronic structure. To model highly correlated materials correctly, a number of methods have been developed: the self-interaction correction method,<sup>30</sup> modified DFT (DFT + U),<sup>31–35</sup> dynamic mean field theory,<sup>36</sup> and hybrid density functionals.<sup>37–39</sup> As a computationally tractable method, DFT + U offers a means of study in which the electronic structure can be computed. In the Liechtenstein DFT + U formalism, independent Coulomb (U) and exchange (J) terms treat the on-site Coulomb repulsion of the An f-electrons. The values are derived from higher level ab initio methods or obtained through semiempirical analysis.<sup>26</sup>

The electronic structure of  $\text{AnO}_2$  is influenced by changes in the magnetic order;<sup>27</sup> here, the importance of magnetic vector reorientation is highlighted. The effect of transverse 3k

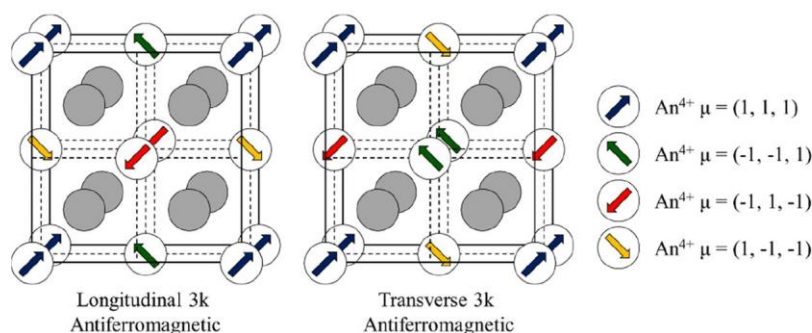


Figure 1. Longitudinal 3k AFM and transverse 3k AFM phases for the AnO<sub>2</sub> crystal structure.

antiferromagnetic (AFM) behavior on the properties of the UO<sub>2</sub> surface is unknown, whereas investigations on NpO<sub>2</sub> and PuO<sub>2</sub> surfaces are even less common.<sup>9,11</sup> Information on the low-index AnO<sub>2</sub>(111), (011), and (001) surfaces has been calculated by DFT + U: energetics, ionic relaxation, electrostatic isosurfaces, scanning tunneling microscopy (STM) images, crystal morphology, and dipolar reconstructions.

**1.1. Magnetic Structure.** The magnetic structure of AnO<sub>2</sub> is highly complicated. A discontinuous first-order magnetic phase transition ( $T_N = 30.8$  K)<sup>40</sup> in UO<sub>2</sub> has been established by heat capacity,<sup>41,42</sup> magnetic susceptibility,<sup>43</sup> and neutron diffraction<sup>44–46</sup> measurements. A transverse 3k AFM ground state has been identified (Figure 1).<sup>26,29,47,48</sup> The ground state corresponds to an internal  $\text{Pa}\bar{3}(\text{no. 205})$  crystallographic distortion synonymous with the magnetic order (the displacement of O<sup>2-</sup> ions is 0.014 Å).<sup>46,47,49,50</sup>

The magnetic structure of NpO<sub>2</sub> remains unresolved. In the absence of interactions that break time-reversal symmetry conditions, the Np<sup>4+</sup> ion (a Kramers ion, one with an uneven number of valence electrons) should order magnetically at low temperature.<sup>51</sup> A first-order paramagnetic (PM)–AFM phase transition ( $T = 25.4$  K) has been inferred by magnetic susceptibility<sup>52</sup> and specific heat capacity measurements.<sup>53,54</sup> In spite of an exhaustive search, a measurable local magnetic moment has not been identified by low-temperature Mössbauer ( $T = 1.5$  K),<sup>51</sup> neutron diffraction ( $12 \text{ K} < T < 30 \text{ K}$ ),<sup>55</sup> and muon spin rotation ( $0.3 \text{ K} < T < 25.4 \text{ K}$ ) measurements.<sup>56,57</sup>

In terms of the crystal structure, no evidence has been found of an external distortion, which would indicate a noncollinear 3k AFM order.<sup>54</sup> An internal O<sup>2-</sup> ion distortion [indicative of transverse 3k AFM behavior with  $\text{Pa}\bar{3}(\text{no. 205})$  crystal symmetry] can be inferred from the small broadening of Mössbauer spectroscopic lines<sup>51</sup> and inelastic neutron scattering (INS) ( $5 \text{ K} < T < 25 \text{ K}$ ) measurements.<sup>58,59</sup> An internal O<sup>2-</sup> ion distortion of 0.02 Å has been calculated, which is, however, below the experimental resolution.<sup>54,57,60</sup> In contrast, a longitudinal 3k AFM ground state has been indicated by resonant X-ray scattering<sup>61</sup> ( $10 \text{ K} < T < 17 \text{ K}$ ) and <sup>17</sup>O nuclear magnetic resonance (NMR) measurements ( $T = 17 \text{ K}$ ).<sup>62</sup> The transverse 3k AFM state, relative to the longitudinal 3k AFM state, is 0.002 eV·formula unit<sup>-1</sup> lower in energy (as calculated by HSE06 incorporating SOI).

An experimental singlet  $\Gamma_1$  diamagnetic PuO<sub>2</sub> ground state has been inferred from: magnetic susceptibility ( $T = 4 \text{ K}$ ), INS ( $T > 30 \text{ K}$ ), and NMR ( $T > 4 \text{ K}$ ) measurements. However, a number of inconsistencies have been identified, and an ordered magnetic ground state can be assumed.<sup>27</sup> In contrast to experimental measurements, a longitudinal 3k AFM ground state has been calculated.<sup>18,22–24,39,63–73</sup> It is thought that PuO<sub>2</sub>

could be a small-moment insulator (similar to NpO<sub>2</sub>) for which DFT overestimates the magnetic moments. In this study, the transverse 3k AFM order (UO<sub>2</sub> and NpO<sub>2</sub>) and the longitudinal 3k AFM order (PuO<sub>2</sub>) have been used to describe the crystals.

To model the noncollinear magnetic behavior, it is imperative that relativistic effects are considered. A considerable number of studies ignore the SOI (important in heavy-fermion systems) to reduce the computational cost.<sup>11,74–76</sup> A limited number of studies on UO<sub>2</sub><sup>9</sup> and PuO<sub>2</sub><sup>23</sup> consider relativistic contributions to the total energy. The importance of SOI on modeling UO<sub>2</sub> by DFT initially seemed to be inconsequential.<sup>9</sup> In a nonrelativistic treatment of other actinide systems, the study has often been cited to justify the absence of SOI.<sup>9,23,74</sup> The importance of SOI on the PuO<sub>2</sub>(111) surface energies has now been highlighted by hybrid DFT,<sup>23</sup> but all studies have limited themselves to a discussion of the collinear 1k AFM order.

A major limitation of scalar calculations is the inability to orient the magnetic moments relative to the direction of the surface. In this manner, the magnetic moments are directed orthogonal to the surface plane, which leads to notable inconsistencies within the electronic structure.<sup>27,29</sup> If not corrected, the orientation of the magnetic field is also directed orthogonal to the surface plane because the principal axis differs between the surfaces. Consequently, the electronic, magnetic, and crystal structures differ between the bulk crystal structure and individual surfaces. If the magnetic vectors are not reoriented, the energetics and structural relaxations derived by this approach are incomplete.<sup>27</sup> This is particularly concerning when calculating the surface energy, which is derived from the bulk structure, and it is therefore important that the magnetic vectors relative to the surface are carefully reoriented. In the past studies where this essential transformation has been omitted, the energies of the bulk and surface are therefore often incomparable, which introduces a significant error when calculating the energy of the surface. In this study, the magnetic vectors are reoriented relative to the surface plane, which ensures that we preserve the noncollinear 3k AFM structure. In addition, the reduction of cubic symmetry associated with collinear 1k AFM states (used in past calculations) is avoided.<sup>27</sup>

The magnetic structure is commonly defined by the principal axis. The principal axis of the AnO<sub>2</sub> (111) and (011) surfaces differs from that of the bulk crystal, and the final magnetic, electronic, and crystal structures are therefore inequivalent. However, this is not the case for the AnO<sub>2</sub>(001) surface which shares the same axes. To illustrate in a two-dimensional material, we consider the first two layers of a collinear 1k AFM material (Figure 2). The (01) surface and the crystal share the same principal axis, and the magnetic structures are therefore directly related. In the (11) surface, the principal axis differs from that of



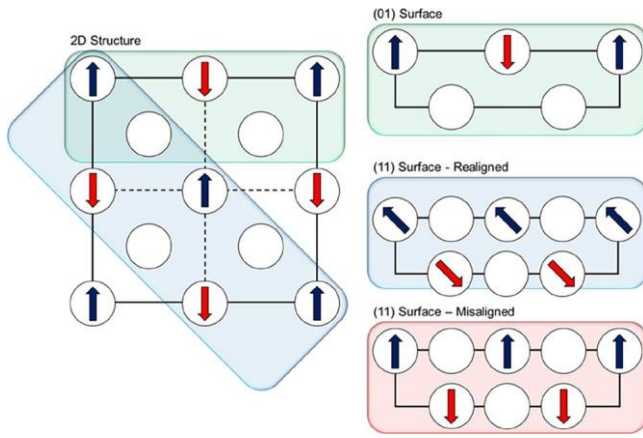


Figure 2. Surface magnetism of a two-dimensional material. The direction of the magnetic moments for the respective surfaces is shown for the first two layers of the bulk crystal structure. The highlighted (01) (green) and (11) (blue) surfaces correctly emulate the magnetic structure in the bulk crystal. In contrast, the (11) (red) surface illustrates an incorrect depiction where the magnetic moments are aligned orthogonal to the surface.

the crystal, which results in an unrelated magnetic and electronic structure. It is therefore critical to orient the magnetic vectors to emulate the initial crystal structure.

## 2. COMPUTATIONAL METHODOLOGY

**2.1. Calculation Details.** A noncollinear relativistic computational study of  $\text{AnO}_2$  ( $\text{An} = \text{U}, \text{Np}, \text{or Pu}$ ) surfaces has been completed with the Vienna Ab initio Simulation Package.<sup>30,36,77</sup> The code uses planewave basis sets, relativistic effective core potentials, and frozen-core projector-augmented wave (PAW) method. The cutoff energy of the planewave basis set is 500 eV. The uranium ( $6s^2, 7s^2, 6p^6, 6d^2, 5f^2$ ), neptunium ( $6s^2, 7s^2, 6p^6, 6d^2, 5f^3$ ), plutonium ( $6s^2, 7s^2, 6p^6, 6d^2, 5f^4$ ), and oxygen ( $2s^2, 2p^4$ ) valence electrons have been explicitly considered. The integration over the Brillouin zone is completed with the Blöchl tetrahedron method and a  $\Gamma$ -centered k-point grid.<sup>78,79</sup> The influence of the SOI<sup>74</sup> and noncollinear magnetic wave vectors has been considered. As a correction to the total energy, the SOI is included as a final perturbation. In the treatment of the SOI term, a few assumptions are made. First, a complete basis set is formed within the PAW spheres, and the SOI outside of the PAW spheres is irrelevant.<sup>74</sup> Second, the wave functions are solutions of the radial scalar relativistic Schrödinger equation, which includes Darwin and mass velocity terms. The spin quantization axis is defined by the (001) plane, from which magnetic and spinorlike values are calculated.

The on-site Coulomb repulsion of the  $\text{An } 5f$  electrons has been treated by the Liechtenstein et al. DFT +  $U$ <sup>33–35</sup> formalism.<sup>34</sup> In the Liechtenstein et al. formalism, the Coulomb ( $U$ ) and exchange ( $J$ ) modifiers are treated as independent variables.<sup>34</sup> To correctly calculate the electronic structure of  $\text{AnO}_2$  (where conventional methods often fail), the Coulomb modifier has been chosen to emulate the experimental band gap. The uranium ( $U = 3.35$  eV), neptunium ( $U = 4.25$  eV), and plutonium ( $U = 6.00$  eV) Coulomb modifiers are shown.<sup>27,29</sup> The influence of  $J$  on noncollinear magnetic materials has been investigated.<sup>26,27,80</sup> The anisotropic nature of the  $f$ -states has been shown to increase with  $J$  (and with  $U$ ), and therefore  $J$  is ignored in this study.<sup>26,80,81</sup> The selected conditions offer an accurate representation of the electronic structure. The

exchange-correlation energy has been evaluated by the revised Perdew–Burke–Ernzerhof for solids (PBEsol) function-al.<sup>31,32,82</sup> The iteration threshold for electronic and ionic convergences has been set at  $1 \times 10^{-5}$  eV and  $1 \times 10^{-2}$  eV  $\text{\AA}^{-1}$ , respectively. As the crystal and electronic structures of  $\text{AnO}_2$  are highly dependent on the magnetic state, it is imperative to correctly reorientate the magnetic vectors with respect to the surface plane.

Ionic relaxation is a common mechanism by which the surface energy is minimized with respect to the unrelaxed surface. The surface energy ( $\gamma$ ) is a measure of the surface stability and is defined by

$$\gamma = \frac{E_{\text{tot}}(N) - N \cdot E_{\text{AnO}_2}}{2A} \quad (1)$$

The number of formula units ( $N$ ), the total energy of the surface slab,  $[E_{\text{tot}}(N)]$ , and the total energy per formula unit ( $E_{\text{AnO}_2}$ ) are defined in the parentheses. In our calculations, all ions are relaxed, whereas the dimensions of the unit cell are fixed. The conjugate gradient method has been employed in the relaxation of the ions. Images are visualized by the Crystal-Maker<sup>83</sup> and VESTA codes.<sup>84</sup> The density of states have been illustrated by the SUMO code, a command-line plotting tool for ab initio calculations.<sup>85</sup>

**2.2. Low-Index Surface Models.** The low-index  $\text{AnO}_2$  (111), (011), and (001) surfaces are created by the METADISE code (Figure 3)<sup>86</sup> from the ionically relaxed crystal structure.

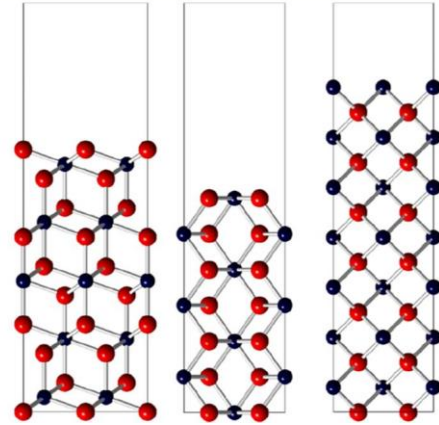


Figure 3. Low-index  $\text{AnO}_2$ (111), (011), and (001) surfaces of an ideal calcium fluoride ( $\text{CaF}_2$ ) structural motif. The oxygen (red) and actinide (blue) ions are indicated.

The nonpolar (111) surface is comprised of charged  $\text{O}-\text{An}-\text{O}$  monolayers, whereas the dipolar (011) surface is comprised of charge neutral planes.

The polar (001) surface (formed of dipolar  $\text{An}-\text{O}$  layers) is inherently unstable.<sup>17,87,88</sup> The electrostatic energy relative to the number of monolayers diverges; this is driven by the electric dipole moment.<sup>89,90</sup> To eliminate the dipole moment, the surface undergoes a reconstruction, whereby half of the charge oxygen ions are transposed from one surface to the other. This results in the formation of a half-filled oxygen terminated surface (Figure 4). The reconstruction is influenced by environmental conditions in nature.<sup>88,91</sup> In the nonpolar reconstructed (001) $\alpha$  or (001) $\beta$  configurations in a (1 $\times$ 1) unit cell can be formed. Although numerous configurations are possible in a (1 $\times$ 2) unit cell, the (001) $\alpha\beta$  reconstruction offers

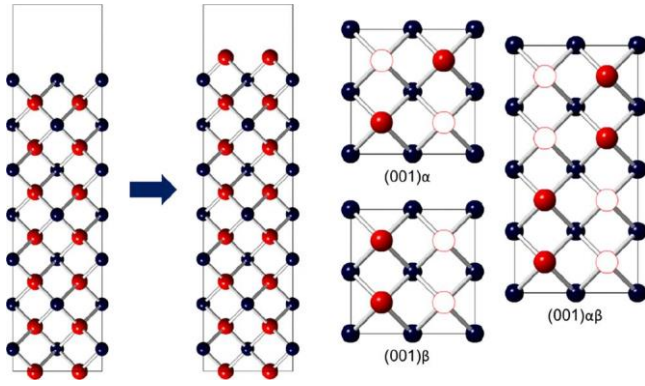


Figure 4. Reconstruction of the AnO<sub>2</sub> (001) surface. In a (1·1) unit cell, the transposition of oxygen ions results in the (001)α or (001)β configurations. In a (1·2) unit cell, the transposition of oxygen ions results in the (001)αβ configuration. The oxygen (red), oxygen vacancies (white), and actinide (blue) ions are indicated.

hybridization between the two (1·1) reconstructions, and in this study, we have calculated the relative stabilities of these three surface configurations.

The surface energy is converged with respect to the k-point grid to under 0.05 J·m<sup>-2</sup> (Figure 5). The (111) surface is calculated from a 5·5·1 Γ-centered k-point grid recommended for hexagonal structures, whereas the (011) and (001) surfaces are calculated from a 4·4·1 Γ-centered k-point grid.<sup>87</sup> To minimize the potential aliasing errors, the initial bulk structure (from which the surfaces are derived) is calculated with both 4·4·4 and a 5·5·5 Γ-centered k-point grids for direct comparison. Finally, the (001)αβ surface is calculated from a 4·2·1 Γ-centered k-point.

**2.3. Hive Code.** In the STM Hive code,<sup>92,93</sup> the Tersoff–Hamann model is considered, where the tunneling current is equivalent to the local density of states.<sup>94</sup> A point source at a constant height (2.5 Å) and a Fermi energy sample bias (−2.50 eV) are used. Topographies calculated by HIVE include copper,<sup>95</sup> germanium,<sup>92,93</sup> gold,<sup>96</sup> iron oxide,<sup>97</sup> and thorium dioxide.<sup>98</sup>

**2.4. Wulff Reconstruction.** According to the Gibbs thermodynamic principle, the equilibrium crystal morphology is influenced by the total surface energy of the medium interface. An equilibrium crystal morphology that minimizes  $G_i$  has been calculated as follows (eq 3)

$$G_i = \sum_j \gamma_j A_j \quad (2)$$

The terms in the parentheses describe the total crystal-medium interface free energy ( $G_i$ ), the surface Gibbs free energy ( $\gamma_j$ ), and the surface area ( $A_j$ ).

### 3. RESULTS AND DISCUSSION

**3.1. Model Constraints.** **3.1.1. Surface Energetics.** As a function of the number of formula units used, the energy of the low-index AnO<sub>2</sub> surfaces has been calculated (Supporting Information, Figure S1). The ions are fully relaxed while keeping the relative dimensions of the unit cell fixed. In this study, the surface energy is converged to within 0.01 J·m<sup>-2</sup> when 12 or more formula units are used. The surface energy increases across the series as (111) < (011) < (001)α < (001)β (typical of fluorite-structured materials) (Table 1).<sup>89,98</sup> The energy differ-

Table 1. Relaxed Energy (J·m<sup>-2</sup>) of the AnO<sub>2</sub>(111), (011), and (001) Surfaces

	(111)	(011)	(001)		
			(001)α	(001)β	(001)αβ
UO <sub>2</sub>	0.85	1.23	1.75	1.83	1.69
NpO <sub>2</sub>	0.90	1.28	1.86	1.92	1.80
PuO <sub>2</sub>	0.92	1.35	1.96	2.13	1.85

ence between the (001)α and (001)β terminations are relatively small in UO<sub>2</sub> (0.08 J·m<sup>-2</sup>) and NpO<sub>2</sub> (0.06 J·m<sup>-2</sup>) compared to PuO<sub>2</sub> (0.19 J·m<sup>-2</sup>). If one uses a (1·1) unit cell model, the (001)α surface relative to the (001)β surface is energetically favorable, which is confirmed independently by an interatomic potential-based investigation on UO<sub>2</sub>.<sup>91</sup> Compared with the past DFT-based methods, the calculated surface energies are considerably greater for each surface,<sup>9,11,17,18,25,76,99</sup> although interatomic potential models<sup>91</sup> and relativistic hybrid calculations<sup>15</sup> of UO<sub>2</sub> have resulted in even higher surface energies.

In addition, interatomic potential models of UO<sub>2</sub> have calculated lower-energy (001) surface reconstructions, which are formed using a larger unit cell.<sup>91,100</sup> In the reconstruction of the (001) surface in our (1·1) unit cell, only the (001)α and (001)β configurations can be generated, whereas the surface energy of the (001)αβ configuration from a (1·2) unit cell (calculated using 28 formula units) relative to the (001)α and (001)β configurations is considerably lower in energy (Table 1). This implies a limitation of the DFT (1·1) unit cell model, and it is clearly possible that other configurations, even in larger cells, could be more stable. However, increasing the size of the cell

increases the computational cost of the system significantly, and

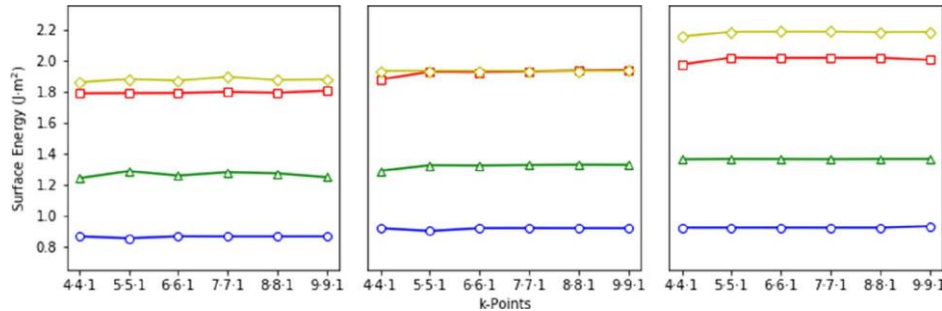


Figure 5. Surface energy converged with respect to the k-point grid for each surface: (a) uranium dioxide, (b) neptunium dioxide, and (c) plutonium dioxide. The colors indicate the (111) (green), (011) (blue), (001)α (red), and (001)β (yellow) surfaces. In these calculations, the (111), (001)α, and (001)β surfaces are formed of 15 monolayers, whereas the (011) surface is formed of 7 monolayers.

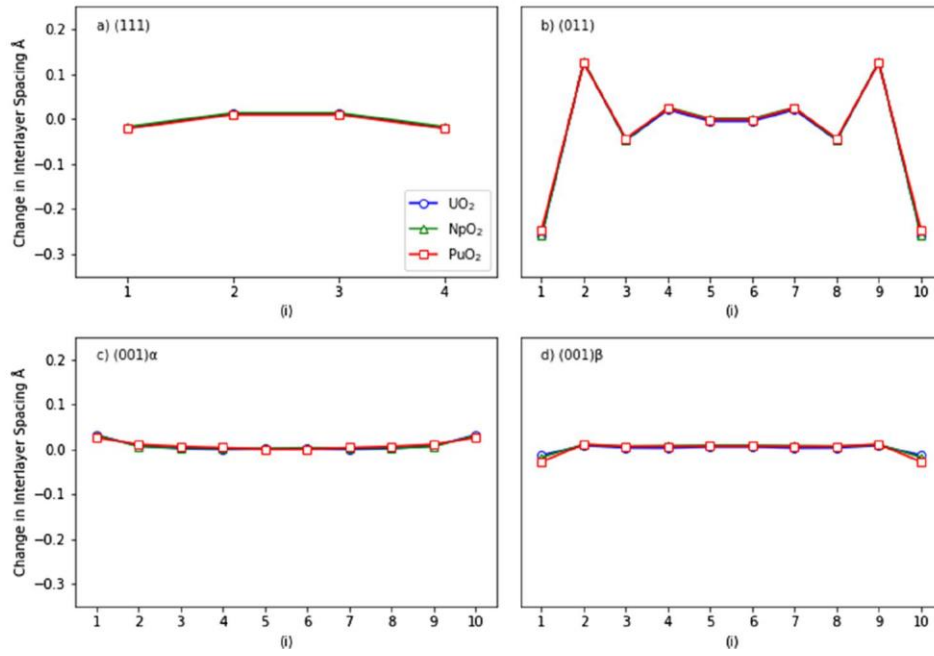


Figure 6. Interlayer An–An relaxation for (a) (111), (b) (011), (c) (001)α, and (d) (001)β surfaces. The interlayer spacing index (i) is indicated in the parentheses.

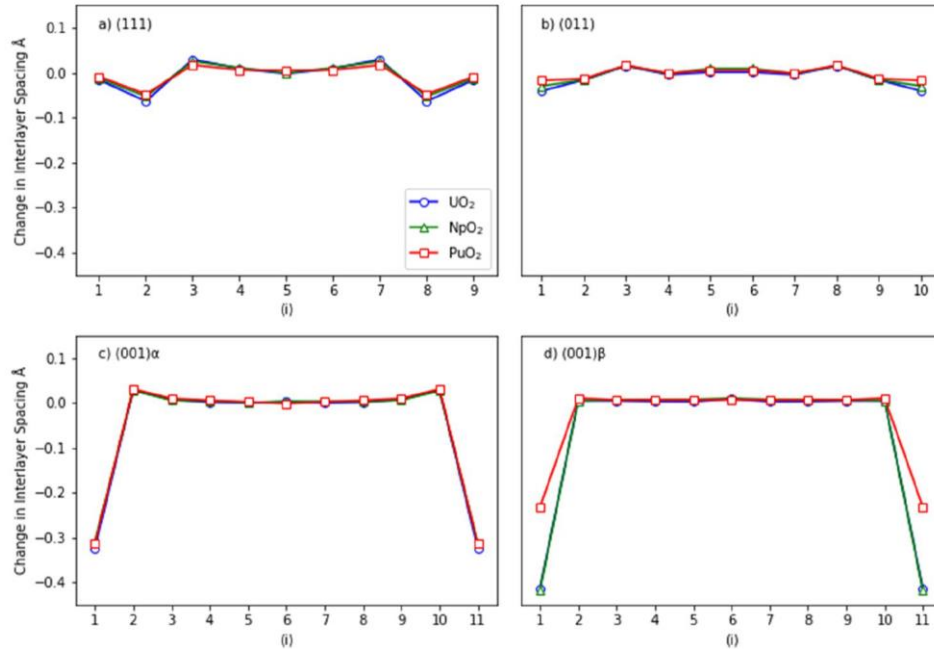


Figure 7. Interlayer O–O relaxation for (a) (111), (b) (011), (c) (001)α, and (d) (001)β surfaces. The interlayer spacing index (i) is indicated in the parentheses.

a systematic fully relativistic DFT study of bigger simulations cells is currently computationally intractable.

**3.1.2. Ionic Relaxation.** The low-index  $AnO_2$  surfaces are characterized by the changes in the interlayer spacings (Figures 6a–d and 7a–d), which enable a quantitative analysis of the structural relaxation between layers. The interlayer relaxation ( $d_{\text{interlayer}}$ ) is calculated by

$$d_{\text{interlayer}} = (d_{i,i+1})_{\text{relaxed}} - d_{\text{unrelaxed}} \quad (3)$$

where  $(d_{i,i+1})_{\text{relaxed}}$  is the average interlayer separation of ions in the relaxed surface and  $d_{\text{unrelaxed}}$  is the average interlayer

separation of ions in the unrelaxed surface. The interlayer relaxation is reminiscent of studies on the isostructural  $CeO_2$  material, with similar results found for the (111) and (011) surfaces.<sup>101</sup>

In the context of An–An relaxation, the (111) surface is marginally distorted. The major difference is confined to the oxygen separation in the second interlayer space. The (011) surface undergoes the greatest overall interlayer relaxation, with the first surface layer experiencing a marked contraction, where the first An layer contracts significantly more than the first O layer. The contraction of the first layer is countered by a slight



expansion of An ions in the second layer, but the bulk structure is regained by the fifth layer. The terminal O ions in the (001) $\alpha$  and (001) $\beta$  surface undergo a significant contraction, although the remainder of the structure is relatively unaffected. In general, the interlayer relaxation is confined to the first 5 Å, indicating that for investigations of surface reactivity, a slab of minimum 10 Å thickness should be used. Our results are similar to those found in studies of CeO<sub>2</sub> and ThO<sub>2</sub>.<sup>98</sup>

In the context of interlayer O–O relaxation, the distortion of the surface is primarily confined to the first three to four monolayers and the degree of ionic relaxation is generally identical in the AnO<sub>2</sub> surfaces, with the exception of the PuO<sub>2</sub>(001) $\beta$  surface. In the PuO<sub>2</sub>(001) $\beta$  surface, the relaxation of the oxygen ions is significantly less relative to the UO<sub>2</sub> and NpO<sub>2</sub>(001) $\beta$  surfaces. Thus, of the (001) $r$  surfaces, the UO<sub>2</sub> and NpO<sub>2</sub>(001) $\beta$  surfaces undergo the greatest surface relaxation, whereas in PuO<sub>2</sub>, the (001) $\alpha$  surface undergoes the greatest surface relaxation, which is a result of the magnetic order and the relaxation in the *xy*-plane.

No significant structural distortion in the *xy*-plane occurs in the AnO<sub>2</sub>(111), (011), or (001) $\alpha$  surface, possibly as a result of preserving the Pa $\bar{3}$ (no. 205) or Fm $\bar{3}$ m (no. 225) cubic symmetry from the use of noncollinear 3k AFM order.<sup>27</sup> In contrast, the oxygen ions in the UO<sub>2</sub> and NpO<sub>2</sub>(001) $\beta$  configuration are shifted from their initial positions by the use of transverse 3k AFM ordering (Figure 8). This distortion is not

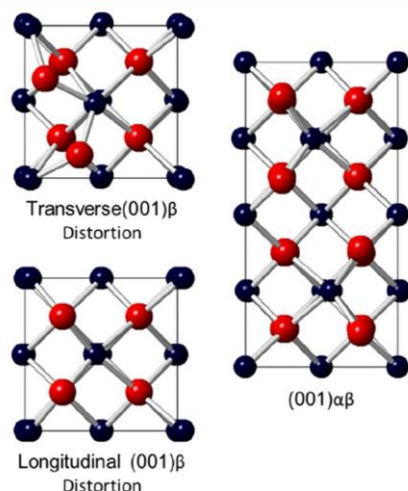


Figure 8. Ionic relaxation of the low-index AnO<sub>2</sub>(001) reconstructed surfaces. The transverse (001) $\beta$  surface is representative of transverse 3k AFM behavior for UO<sub>2</sub> and NpO<sub>2</sub>, whereas the longitudinal (001) $\beta$  surface is representative of longitudinal 3k AFM behavior in PuO<sub>2</sub>. The hybridized (001) $\alpha\beta$  surface is calculated regardless of the magnetic order for AnO<sub>2</sub>. The oxygen (red) and actinide (blue) ions are indicated.

observed in the corresponding PuO<sub>2</sub> surface in which the ions are relatively fixed, although there is a minor distortion of the surface plutonium ions, potentially as a consequence of using either transverse 3k AFM or longitudinal 3k AFM behavior. By comparison, the oxygen ions in the (001) $\alpha\beta$  configuration are relatively static, and instead, the actinide ion is partially shifted toward the terminal oxygen ions.

**3.2. Surface Properties.** **3.2.1. Electronic Structure.** The electronic structure of the AnO<sub>2</sub> surfaces has been calculated (Figure 9). The covalent nature of the AnO<sub>2</sub> materials (a consequence of An (f) and O (p) mixing) is seen to increase

along the series. The Mott–Hubbard insulating nature of UO<sub>2</sub> is characterized by transitions primarily occurring across the An f-bands. Compared to relativistic hybrid DFT calculations of UO<sub>2</sub>, the calculated band gaps for the low-index surfaces are considerably greater.<sup>15</sup> The charge-transfer insulating nature of PuO<sub>2</sub> is characterized by transitions primarily between the valence Pu f-band and the conduction O p-band. In NpO<sub>2</sub>, both Mott insulating and charge-transfer characteristics are shown in the surface. In general, the electronic structure is only partially perturbed between surfaces.

In addition, the electron affinity and ionization potential of the AnO<sub>2</sub> surfaces has been calculated (Table 2). This information fills a significant gap in the literature where X-ray photoelectron spectroscopy and Kelvin probe microscopy studies are yet to be performed. The electron affinity and the ionization potential increase along the (011) < (111) < (001) $\beta$  < (001) $\alpha$  series. Of the AnO<sub>2</sub> (An = U, Np, or Pu) materials, UO<sub>2</sub> is the least reactive, whereas PuO<sub>2</sub> is the most reactive.

**3.2.2. Magnetic Deviation.** The magnetic structure of the low-index AnO<sub>2</sub> surfaces has been investigated. A complete analysis of the actinide ions can be found in the [Supporting Information](#). The localized magnetic normalized root-mean-square deviation (nrmsd) of the first three monolayers has been calculated for each surface (Figure 10). As the monolayer surface depth increases, the magnetic distortion decreases. The total magnetic moment of U (1.37  $\mu_B \cdot \text{ion}^{-1}$ ), Np (2.70  $\mu_B \cdot \text{ion}^{-1}$ ), and Pu (3.80  $\mu_B \cdot \text{ion}^{-1}$ ) ions remains constant.

The comparative localized magnetic deviation in NpO<sub>2</sub> for identical surfaces is relatively high. A number of competing low-temperature ( $T < 25.4$  K) magnetic states could cause the distortion. For instance, the transverse 3k AFM state, relative to the ferromagnetic (FM) (111) ground state, is 0.002 eV per formula unit higher in energy; however, no experimental evidence of a FM (111) ground state, which results in a R $\bar{3}$ m (no. 166) crystallographic distortion, exists.<sup>25</sup> In addition, the localized magnetic deviation of the (001) $\alpha$  series can be ascribed to the surface instability. In the first three monolayers of the (001) $\alpha$  surface, a FM and an AFM domain are formed. The lowest rmsd is found for the PuO<sub>2</sub>(011) surface.

**3.2.3. STM.** The surface energies of UO<sub>2</sub> are extremely sensitive to stoichiometry, defect chemistry, and environmental conditions.<sup>102–104</sup> Low-energy electron diffraction measurements of the UO<sub>2</sub>(111) surface have identified over 16 individual patterns.<sup>105</sup> To assist the experimental analysis, low-index AnO<sub>2</sub> STM images have been calculated (Figure 11). The resulting images are analogues to experimental STM studies of AnO<sub>2</sub> surfaces;<sup>88,106,107</sup> however, in an STM experiment, ionic positions are influenced by perturbations of the electric field caused by the probe. The calculated resolution relative to an experimental study is therefore considerably greater.

The terminal O<sup>2−</sup> ions are observed in white, whereas the An<sup>4+</sup> ions are considerably darker. The individual AnO<sub>2</sub> (An = U, Np, or Pu) (111), (011), and (001) $\alpha$  surface patterns are indistinct. In the (111) surface, the O<sup>2−</sup> ions result in a hexagonal structure, whereas in the (011) surface, a series of darker channels is observed in one direction. In the (001) $\alpha$  surface, the alignment of the O<sup>2−</sup> ions results in a diamond pattern. As a means of differentiating between compounds, the (001) $\beta$  surface is influenced by the magnetic state. In the transverse 3k AFM state for UO<sub>2</sub> and NpO<sub>2</sub>, the O<sup>2−</sup> channels oscillate continuously, whereas in the longitudinal 3k AFM state for PuO<sub>2</sub>, the O<sup>2−</sup> channels are perfectly linear. In other words, the structures can be differentiated by the transverse 3k AFM

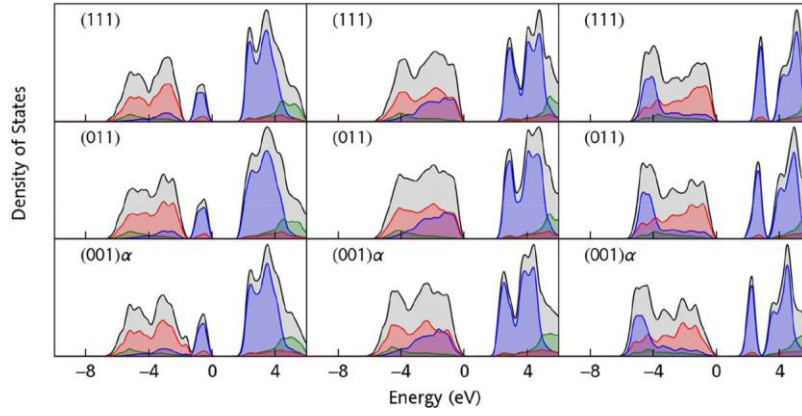


Figure 9. Calculated density of states for the low-index AnO<sub>2</sub>(111), (011), and (001)α surfaces; (left) UO<sub>2</sub>, (center) NpO<sub>2</sub>, and (right) PuO<sub>2</sub>. The colors indicate the actinide f (blue), actinide d (green), and oxygen p (red) bands. The Fermi level is set at 0 eV.

Table 2. Electron Affinity (eV), Ionization Potential (eV), and Surface Energy (J·m<sup>-2</sup>) for the Low-Index AnO<sub>2</sub> Surfaces

		(111)	(011)	(001)α	(001)β
UO <sub>2</sub>	electron affinity (eV)	2.44	1.45	3.69	2.93
	ionization potential (eV)	4.54	3.51	5.75	5.00
	band gap (eV)	2.11	1.96	2.01	2.15
	surface energy (J·m <sup>-2</sup> )	0.85	1.23	1.75	1.83
NpO <sub>2</sub>	electron affinity (eV)	3.11	2.11	4.33	3.45
	ionization potential (eV)	5.98	4.89	7.11	6.23
	band gap (eV)	2.64	2.47	2.14	2.50
	surface energy (J·m <sup>-2</sup> )	0.90	1.28	1.86	1.92
PuO <sub>2</sub>	electron affinity (eV)	3.60	1.74	4.89	4.65
	ionization potential (eV)	6.45	4.53	7.67	7.44
	band gap (eV)	2.58	2.12	1.84	2.03
	surface energy (J·m <sup>-2</sup> )	0.92	1.35	1.96	2.13

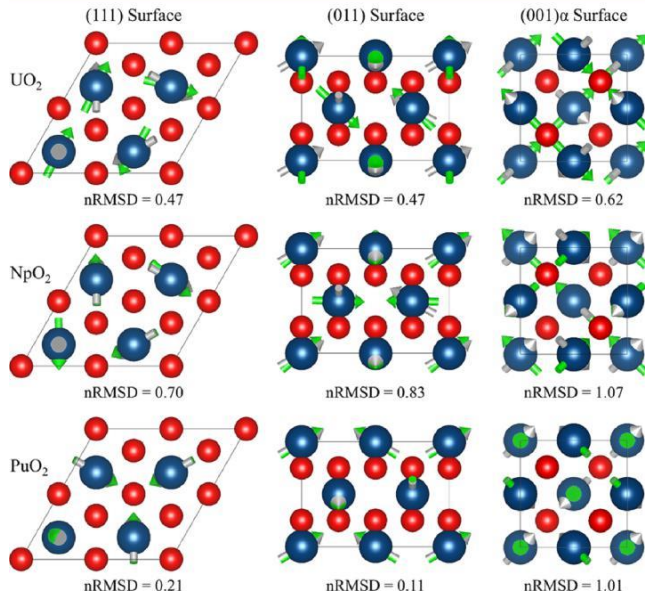


Figure 10. Cross-sectional illustration of the AnO<sub>2</sub>(111), (011), and (001)α surfaces for the first three monolayers. The initial magnetic (silver) and relaxed magnetic (green) vectors are colored. The actinide (blue) and oxygen (red) ions are also shown.

state of UO<sub>2</sub> and NpO<sub>2</sub> or by the longitudinal 3k AFM state of PuO<sub>2</sub>, which is useful information for comparison with future experimental patterns to deduce the magnetic states.

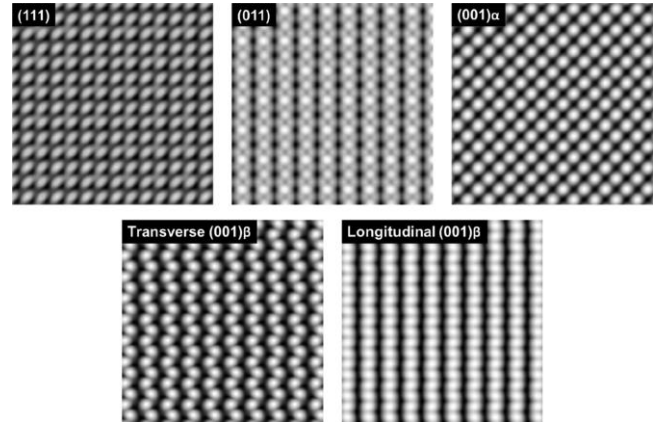


Figure 11. Low-index STM images. AnO<sub>2</sub>(111), (011), and (001)α are indistinguishable. The transverse (001)β surface is found for UO<sub>2</sub> and NpO<sub>2</sub>, whereas the longitudinal (001)β surface is found for PuO<sub>2</sub>. The terminal O<sup>2-</sup> ions are observed in white; the An<sup>4+</sup> ions are in dark gray.

3.2.4. Electrostatic Potential Isosurface. The electrostatic potential isosurface for the low-index AnO<sub>2</sub> surfaces has been calculated using the PBEsol + U functional (Figure 12), where the colors indicate the regions of relative high (red) and low (blue)

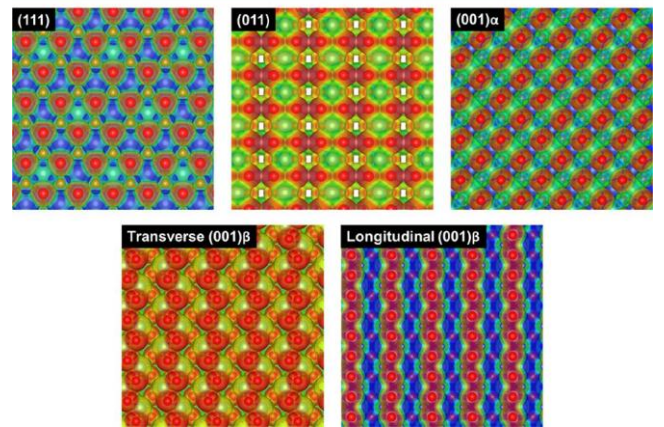


Figure 12. Electrostatic potential isosurfaces. AnO<sub>2</sub>(111), (011), and (001)α are indistinguishable. Transverse (001)β surface is found for UO<sub>2</sub> and NpO<sub>2</sub>, whereas the longitudinal (001)β surface is found for PuO<sub>2</sub>. The regions of high (red) and low (blue) electrostatic potential are indicated.



(blue) charge densities. An interesting region of high charge density for an An ion (highlighted in light blue) on the (111) surface has been identified. The area is expected to have a different reaction chemistry compared to the remaining An ions, possibly a site of catalytic activity. In general, regions of high charge density are localized near the oxygen ions. The electrostatic potential isosurfaces of  $\text{UO}_2$  and  $\text{NpO}_2(001)\beta$  differ from that of the  $\text{PuO}_2(001)\beta$  surface as a consequence of the surface ionic relaxation in the xy-plane, and the surfaces are therefore expected to have different chemical activities.

**3.2.5. Crystal Morphology.** Low-voltage scanning electron microscopy of  $\text{UO}_2$  shows a truncated octahedral Wulff crystal morphology,<sup>108</sup> which to our knowledge is the only experimental study concerning the morphology. The truncated octahedral Wulff crystal morphology of  $\text{UO}_2$  is inconsistent with studies of other fluorite-type crystal structures and may be the result of environmental influences and the method of sample preparation. The crystals were formed under high pressure (400 MPa) and temperature (1700 °C). A truncated octahedral  $\text{UO}_2$  Wulff crystal morphology ( $\gamma_{100} = 1.60 \pm 0.02 \text{ J}\cdot\text{m}^{-2}$ ,  $\gamma_{111} = 1.14 \pm 0.03 \text{ J}\cdot\text{m}^{-2}$ ) has been found; where, empirical interatomic potentials without periodical boundary conditions have been used.<sup>109</sup>

In this study, an octahedral Wulff crystal morphology has been calculated (Figure 13) from the surface energies of the low-index



Figure 13.  $\text{AnO}_2$  Wulff reconstruction. The crystal structure is formed of (111) facets.

(111), (011), and (001) $\alpha\beta$  surfaces only. As a result of their relative instabilities, the (001) $\alpha$  and (001) $\beta$  surfaces are omitted. Indeed, other high-index surfaces are considerably greater in energy, and their influence on the Wulff crystal morphology is assumed to be negligible.

In terms of computational theory, calculations have shown that the crystal structure is influenced by the magnetic state.<sup>26,27</sup> In theory, the low-temperature octahedral Wulff crystal morphology is linked to the noncollinear 3k AFM state, whereas the high-temperature truncated octahedral Wulff crystal morphology is linked to the PM state. In contrast, the octahedral Wulff crystal morphology of the  $\text{AnO}_2$  materials is consistent with that of fluorite-based materials. The octahedral morphology in the present study is also consistent with: past DFT ( $\text{PuO}_2$ ,<sup>22</sup>  $\text{NpO}_2$ <sup>98</sup>) and interatomic potential calculations.<sup>91</sup> The (111) surface dominates the morphological features of the particle.

Interatomic potential models of the  $\text{UO}_2(001)$  surface have indicated surface configurations of lower energy in a (2·2) unit cell, however this energy is not sufficiently low enough to result

in a truncated octahedron.<sup>91</sup> In the calculation of (001) surface energetics, the major limitation is the size of the unit cell, and hence there is a possibility that larger cells may result in a configuration of sufficiently low energy to result in a truncated octahedron. In this study, we have used a (1·1) unit cell with either the (001) $\alpha$  or (001) $\beta$  configuration, although additional configurations are possible in larger supercells. In theory, one of these surfaces may possess sufficiently low energy to affect the morphology. However, a systematic investigation of the (2·2) surface is computationally unfeasible because of the large number of compute-intensive configurations that must be explored.

In another scenario, the experimental sensitivity of  $\text{UO}_2$  resulted in a crystal morphology influenced by environmental conditions. It is known that the interaction of oxygen with the  $\text{AnO}_2$  surfaces influences the composition range of the solid and the formation of superficial structures.<sup>105</sup> In the past, DFT + U studies have indicated that the truncated crystal morphology is the result of oxygen-rich conditions at 300 K.<sup>110</sup> In addition, interatomic potentials indicate that the  $\text{AnO}_2(001)$  surface energy is reduced by hydroxylation,<sup>12,17</sup> which also results in a truncated octahedron. Other models which use interatomic potentials have obtained an octahedral morphology at thermodynamic equilibrium; however, these studies concluded that the truncated morphology is the result of kinetic limitations.<sup>111</sup> Finally, numerous experimental investigations have shown that the surface energies are temperature-depend-

ent.<sup>102,112</sup>

## 4. CONCLUSIONS

PBEsol + U has been used to investigate  $\text{AnO}_2$  surfaces. In the past, collinear 1k AFM states were used to model surface structures, but these models predominately use scalar approximations of the crystal electric field, which causes an inability to reorient the magnetic vectors relative to the plane of the surface. Therefore, the magnetic structures differ across surface indices. This study considers noncollinear 3k AFM behavior and SOI contributions to the surface energetics of the low-index  $\text{AnO}_2$  (111), (011), and (011) surfaces. The magnetic field is carefully reoriented relative to the plane of the surface for a complete description of the magnetic surface structure. Localized magnetic distortions have also been identified.

The interlayer relaxation of the (111), (011), and (001) $\alpha$  surfaces is confined to the first 5 Å. In contrast to past DFT investigations, our surface energies are considerably higher,<sup>11,76</sup> which illustrates the important contribution of the SOI<sup>74</sup> to the calculated surface energetics. Our surface energies suggest that the chemical reactivity of the surface has previously been underestimated. The surface stability increases across the (001) $\beta$  < (001) $\alpha$  < (011) < (111) series, which is typical of  $\text{CaF}_2$ -type structures. From our Wulff reconstruction, the octahedral crystal morphology is completely dominated by (111) facets. As stated, this is consistent with previous calculations of fluorite-type structures. A computationally tractable method to model the low-index  $\text{AnO}_2$  surfaces with improved energetics has been shown.<sup>25</sup> Finally, the models developed and described in this work could be employed in the implementation and use of machine learning methods to investigate structural defects and radiation damage in nuclear fuels.

## ASSOCIATED CONTENT

### \* Supporting Information

The Supporting Information is available free of charge on the ACS Publications website at DOI: 10.1021/acs.jpcc.8b07823.

Monolayer surface energetics, fixed unit cell dimensions, initial magnetic structure, structural ionic relaxation, and magnetic deviation (PDF)

## AUTHOR INFORMATION

Corresponding Author

\*E-mail: uccajtp@ucl.ac.uk.

ORCID

James T. Pegg: 0000-0002-6743-8651

David O. Scanlon: 0000-0001-9174-8601

Nora H. de Leeuw: 0000-0002-8271-0545

Notes

The authors declare no competing financial interest.

## ACKNOWLEDGMENTS

This research was supported by the UK Engineering & Physical Science Research Council (EPSRC) (grant nos. EP/G036675 and EP/K016288) and the Atomic Weapons Establishment Ltd (AWE). A.E.S. gratefully acknowledges the United States Department of Homeland Security (DHS), Domestic Nuclear Detection Office (DNDO), and National Technical Nuclear Forensics Centre (NTNFC) for a postdoctoral research fellowship. N.H.d.L. thanks the Royal Society for an industry fellowship and AWE for a William Penney fellowship. This work made use of the ARCHER UK National Supercomputing Service (<http://www.archer.ac.uk>) via our membership of the UK's HEC Materials Chemistry Consortium, which is funded by EPSRC (EP/L000202).

## REFERENCES

- (1) Haschke, J. M. Corrosion of Uranium in Air and Water Vapor: Consequences for Environmental Dispersal. *J. Alloys Compd.* 1998, 278, 149–160.
- (2) Haschke, J. M.; Allen, T. H. Plutonium Hydride, Sesquioxide and Monoxide Monohydride: Pyrophoricity and Catalysis of Plutonium Corrosion. *J. Alloys Compd.* 2001, 320, 58–71.
- (3) Haschke, J. M.; Allen, T. H.; Martz, J. C. Oxidation Kinetics of Plutonium in Air: Consequences for Environmental Dispersal. *J. Alloys Compd.* 1998, 271–273, 211–215.
- (4) Haschke, J. M.; Allen, T. H.; Morales, L. A. Reactions of Plutonium Dioxide with Water and Hydrogen–Oxygen Mixtures: Mechanisms for Corrosion of Uranium and Plutonium. *J. Alloys Compd.* 2001, 314, 78–91.
- (5) Haschke, J. M.; Allen, T. H.; Morales, L. A. Surface and Corrosion Chemistry of Plutonium. *Los Alamos Sci.* 2000, 26 (2), 252–73.
- (6) Haschke, J. M.; Allen, T. H.; Stakebake, J. L. Reaction Kinetics of Plutonium with Oxygen, Water and Humid Air: Moisture Enhancement of the Corrosion Rate. *J. Alloys Compd.* 1996, 243, 23–35.
- (7) Haschke, J. M.; Martz, J. C. Catalyzed Corrosion of Plutonium: Hazards and Applications. *Los Alamos Sci.* 2000, 26, 266–7.
- (8) Policastro, S.; Martin, F.; Natishan, P.; Moran, P. Corrosion and Corrosion Control. *Kirk-Othmer Encyclopedia of Chemical Technology*; John Wiley & Sons, Inc., 2000.
- (9) Rak, Z.; Ewing, R. C.; Becker, U. Hydroxylation-Induced Surface Stability of  $\text{AnO}_2$  ( $\text{An} = \text{U}, \text{Np}, \text{Pu}$ ) from First-Principles. *Surf. Sci.* 2013, 608, 180–187.
- (10) Ewing, R. C.; Runde, W.; Albrecht-Schmitt, T. E. Environmental Impact of the Nuclear Fuel Cycle: Fate of Actinides. *MRS Bull.* 2010, 35, 859–866.
- (11) Bo, T.; Lan, J.-H.; Zhao, Y.-L.; Zhang, Y.-J.; He, C.-H.; Chai, Z.-F.; Shi, W.-Q. Surface Properties of  $\text{NpO}_2$  and Water Reacting with Stoichiometric and Reduced  $\text{NpO}_2$  (111), (110), and (100) Surfaces From Ab Initio Atomistic Thermodynamics. *Surf. Sci.* 2016, 644, 153–164.
- (12) Abramowski, M.; Redfern, S. E.; Grimes, R. W.; Owens, S. Modification of  $\text{UO}_2$  Crystal Morphologies through Hydroxylation. *Surf. Sci.* 2001, 490, 415–420.
- (13) Cakir, P.; Eloirdi, R.; Huber, F.; Konings, R. J. M.; Gouder, T. Surface Reduction of Neptunium Dioxide and Uranium Mixed Oxides with Plutonium and Thorium by Photocatalytic Reaction with Ice. *J. Phys. Chem. C* 2015, 119, 1330–1337.
- (14) Katz, J. J. *The Chemistry of the Actinide and Transactinide Elements*; Springer Science & Business Media, 2007; Vol. 1.
- (15) Hoover, M. E.; Atta-Fynn, R.; Ray, A. K. Surface Properties of Uranium Dioxide from First Principles. *J. Nucl. Mater.* 2014, 452, 479–485.
- (16) Matzke, H. *Science of Advanced LMFBR Fuels*; Elsevier Science Pub. Co. Inc.: New York, NY, 1986; p 740.
- (17) Tan, A. H. H.; Grimes, R. W.; Owens, S. Structures of  $\text{UO}_2$  and  $\text{PuO}_2$  Surfaces with Hydroxide Coverage. *J. Nucl. Mater.* 2005, 344, 13–16.
- (18) Sun, B.; Liu, H.; Song, H.; Zhang, G.; Zheng, H.; Zhao, X.; Zhang, P. First-Principles Study of Surface Properties of  $\text{PuO}_2$ : Effects of Thickness and O-Vacancy on Surface Stability and Chemical Activity. *J. Nucl. Mater.* 2012, 426, 139–147.
- (19) Wu, X.; Ray, A. K. A Density Functional Study of Plutonium Dioxide. *Eur. Phys. J. B* 2001, 19, 345–351.
- (20) Sun, B.; Zhang, P.; Zhao, X.-G. First-Principles Local Density Approximation+U and Generalized Gradient Approximation+U Study of Plutonium Oxides. *J. Chem. Phys.* 2008, 128, 084705.
- (21) Jomard, G.; Bottin, F.; Geneste, G. Water Adsorption and Dissociation on the  $\text{PuO}_2$  (110) Surface. *J. Nucl. Mater.* 2014, 451, 28–34.
- (22) Jomard, G.; Bottin, F. Thermodynamic Stability of  $\text{PuO}_2$  Surfaces: Influence of Electronic Correlations. *Phys. Rev. B: Condens. Matter Mater. Phys.* 2011, 84, 195469.
- (23) Moten, S. A.; Atta-Fynn, R.; Ray, A. K.; Huda, M. N. Size Effects on the Electronic and Magnetic Properties of  $\text{PuO}_2$  (111) Surface. *J. Nucl. Mater.* 2016, 468, 37–45.
- (24) Boettger, J. C.; Ray, A. K. Fully Relativistic Density Functional Calculations on Hydroxylated Actinide Oxide Surfaces. *Int. J. Quantum Chem.* 2002, 90, 1470–1477.
- (25) Pegg, J. T. A Noncollinear Relativistic Computational Study of the Actinide Dioxides and their Interaction with Hydrogen; UCL (University College London), 2018.
- (26) Pegg, J. T.; Aparicio-Angles, X.; Storr, M.; de Leeuw, N. H. DFT +U Study of the Structures and Properties of the Actinide Dioxides. *J. Nucl. Mater.* 2017, 492, 269–278.
- (27) Pegg, J. T.; Shields, A. E.; Storr, M. T.; Wills, A. S.; Scanlon, D. O.; de Leeuw, N. H. Hidden Magnetic Order in Plutonium Dioxide Nuclear Fuel. *Phys. Chem. Chem. Phys.* 2018, 20, 20943–20951.
- (28) van der Laan, G.; Moore, K. T.; Tobin, J. G.; Chung, B. W.; Wall, M. A.; Schwartz, A. J. Applicability of the Spin-Orbit Sum Rule for the Actinide 5f States. *Phys. Rev. Lett.* 2004, 93, 097401.
- (29) Pegg, J. T.; Shields, A. E.; Storr, M. T.; Wills, A. S.; Scanlon, D. O.; de Leeuw, N. H. Magnetic Structure of  $\text{UO}_2$  and  $\text{NpO}_2$  by First-Principle Methods. *Phys. Chem. Chem. Phys.* 2019.
- (30) Perdew, J. P.; Zunger, A. Self-Interaction Correction to Density-Functional Approximations for Many-Electron Systems. *Phys. Rev. B: Condens. Matter Mater. Phys.* 1981, 23, 5048–5079.
- (31) Hohenberg, P.; Kohn, W. Inhomogeneous Electron Gas. *Phys. Rev.* 1964, 136, B864–B871.
- (32) Kohn, W.; Sham, L. J. Self-Consistent Equations Including Exchange and Correlation Effects. *Phys. Rev.* 1965, 140, A1133–A1138.
- (33) Dudarev, S. L.; Botton, G. A.; Savrasov, S. Y.; Humphreys, C. J.; Sutton, A. P. Electron-Energy-Loss Spectra and the Structural Stability of Nickel Oxide: An LSDA+U Study. *Phys. Rev. B: Condens. Matter Mater. Phys.* 1998, 57, 1505–1509.

- (34) Liechtenstein, A. I.; Anisimov, V. I.; Zaanen, J. Density-Functional Theory and Strong Interactions: Orbital Ordering in Mott-Hubbard Insulators. *Phys. Rev. B: Condens. Matter Mater. Phys.* 1995, 52, R5467–R5470.
- (35) Anisimov, V. I.; Zaanen, J.; Andersen, O. K. Band Theory and Mott Insulators: Hubbard U instead of Stoner I. *Phys. Rev. B: Condens. Matter Mater. Phys.* 1991, 44, 943–954.
- (36) Georges, A.; Kotliar, G.; Krauth, W.; Rozenberg, M. J. Dynamical Mean-Field Theory of Strongly Correlated Fermion Systems and the Limit of Infinite Dimensions. *Rev. Mod. Phys.* 1996, 68, 13.
- (37) Adamo, C.; Barone, V. Toward Reliable Density Functional Methods without Adjustable Parameters: The PBE0 Model. *J. Chem. Phys.* 1999, 110, 6158–6170.
- (38) Heyd, J.; Scuseria, G. E.; Ernzerhof, M. Hybrid Functionals Based on a Screened Coulomb Potential. *J. Chem. Phys.* 2003, 118, 8207–8215.
- (39) Prodan, I. D.; Scuseria, G. E.; Martin, R. L. Covalency in the Actinide Dioxides: Systematic Study of the Electronic Properties using Screened Hybrid Density Functional Theory. *Phys. Rev. B: Condens. Matter Mater. Phys.* 2007, 76, 033101.
- (40) Caciuffo, R.; Amoretti, G.; Santini, P.; Lander, G. H.; Kulda, J.; Du Plessis, P. d. V. Magnetic Excitations and Dynamical Jahn-Teller Distortions in  $\text{UO}_2$ . *Phys. Rev. B: Condens. Matter Mater. Phys.* 1999, 59, 13892–13900.
- (41) Jones, W. M.; Gordon, J.; Long, E. A. The Heat Capacities of Uranium, Uranium Trioxide, and Uranium Dioxide from 15°K to 300°K. *J. Chem. Phys.* 1952, 20, 695.
- (42) Huntzicker, J. J.; Westrum, E. F. The Magnetic Transition, Heat Capacity, and Thermodynamic Properties of Uranium Dioxide from 5 to 350 K. *J. Chem. Thermodyn.* 1971, 3, 61–76.
- (43) Arrott, A.; Goldman, J. E. Magnetic Analysis of the Uranium-Oxygen System. *Phys. Rev.* 1957, 108, 948–953.
- (44) Frazer, B. C.; Shirane, G.; Cox, D. E.; Olsen, C. E. Neutron-Diffraction Study of Antiferromagnetism in  $\text{UO}_2$ . *Phys. Rev.* 1965, 140, A1448.
- (45) Frazer, B. C.; Shirane, G.; Cox, D. E.; Olsen, C. E. First-Order Magnetic Transition in  $\text{UO}_2$ . *J. Appl. Phys.* 1966, 37, 1386.
- (46) Faber, J.; Lander, G. H.; Cooper, B. R. Neutron-Diffraction Study of  $\text{UO}_2$ : Observation of an Internal Distortion. *Phys. Rev. Lett.* 1975, 35, 1770–1773.
- (47) Desgranges, L.; Ma, Y.; Garcia, P.; Baldinozzi, G.; Simeone, D.; Fischer, H. E. What Is the Actual Local Crystalline Structure of Uranium Dioxide,  $\text{UO}_2$ ? A New Perspective for the Most Used Nuclear Fuel. *Inorg. Chem.* 2016, 56, 321–326.
- (48) Dorado, B.; Jomard, G.; Freyss, M.; Bertolus, M. Stability of Oxygen Point Defects in  $\text{UO}_2$  by First-Principles DFT+ U Calculations: Occupation Matrix Control and Jahn-Teller Distortion. *Phys. Rev. B: Condens. Matter Mater. Phys.* 2010, 82, 035114.
- (49) Faber, J.; Lander, G. H. Neutron Diffraction Study of  $\text{UO}_2$ : Antiferromagnetic State. *Phys. Rev. B: Solid State* 1976, 14, 1151–1164.
- (50) Ikushima, K.; Tsutsui, S.; Haga, Y.; Yasuoka, H.; Walstedt, R. E.; Masaki, N. M.; Nakamura, A.; Nasu, S.; Onuki, Y. First-Order Phase Transition in  $\text{UO}_2$ :  $^{235}\text{U}$  and  $^{17}\text{O}$  NMR Study. *Phys. Rev. B: Condens. Matter Mater. Phys.* 2001, 63, 104404.
- (51) Friedt, J. M.; Litterst, F. J.; Rebizant, J. 25-K Phase Transition in  $\text{NpO}_2$  from  $^{237}\text{Np}$  Mössbauer Spectroscopy. *Phys. Rev. B: Condens. Matter Mater. Phys.* 1985, 32, 257–263.
- (52) Erdős, P.; Solt, G.; Ołnierz, Z.; Blaise, A.; Fournier, J. M. Magnetic Susceptibility and the Phase Transition of  $\text{NpO}_2$ . *Physica B+C* 1980, 102, 164–170.
- (53) Westrum, E. F. W., Jr.; Hatcher, J. B.; Osborne, D. W. The Entropy and Low Temperature Heat Capacity of Neptunium Dioxide. *J. Chem. Phys.* 1953, 21, 419–423.
- (54) Mannix, D.; Lander, G. H.; Rebizant, J.; Caciuffo, R.; Bernhoeft, N.; Lidström, E.; Vettier, C. Unusual Magnetism of  $\text{NpO}_2$ : A Study with Resonant X-ray Scattering. *Phys. Rev. B: Condens. Matter Mater. Phys.* 1999, 60, 15187–15193.
- (55) Caciuffo, R.; Lander, G. H.; Spirlet, J. C.; Fournier, J. M.; Kuhs, W. F. A Search for Anharmonic Effects in  $\text{NpO}_2$  at Low Temperature by Neutron Diffraction. *Solid State Commun.* 1987, 64, 149–152.
- (56) Kopmann, W.; Litterst, F. J.; Klauß, H.-H.; Hillberg, M.; Wagener, W.; Kalvius, G. M.; Schreier, E.; Burghart, F. J.; Rebizant, J.; Lander, G. H. Magnetic Order in  $\text{NpO}_2$  and  $\text{UO}_2$  Studied by Muon Spin Rotation. *J. Alloys Compd.* 1998, 271–273, 463–466.
- (57) Santini, P.; Lemanski, R.; Erdős, P. Magnetism of Actinide Compounds. *Adv. Phys.* 1999, 48, 537–653.
- (58) Amoretti, G.; Blaise, A.; Caciuffo, R.; Di Cola, D.; Fournier, J. M.; Hutchings, M. T.; Lander, G. H.; Osborn, R.; Severing, A.; Taylor, A. D. Neutron-Scattering Investigation of the Electronic Ground State of Neptunium Dioxide. *J. Phys.: Condens. Matter* 1992, 4, 3459.
- (59) Caciuffo, R.; Amoretti, G.; Fournier, J. M.; Blaise, A.; Osborn, R.; Taylor, A. D.; Larroque, J.; Hutchings, M. T. Evidence of a Lattice Distortion in  $\text{NpO}_2$  below 25 K from Neutron Magnetic Inelastic Scattering. *Solid State Commun.* 1991, 79, 197–200.
- (60) Spirlet, J. C.; Bednarczyk, E.; Rijkeboer, C.; Rizzoli, C.; Rebizant, J.; Vogt, O. Recent Achievements in Single Crystal Growth of Actinide Compounds. *Inorg. Chim. Acta* 1984, 94, 111–112.
- (61) Wilkins, S. B.; Paixao, J. A.; Caciuffo, R.; Javorsky, P.; Wastin, F.; Rebizant, J.; Detlefs, C.; Bernhoeft, N.; Santini, P.; Lander, G. H. Resonant X-Ray Scattering Study of Magnetic-Dipole and Electric-Quadrupole Order in  $\text{U}_{0.75}\text{Np}_{0.25}\text{O}_2$ . *Phys. Rev. B: Condens. Matter Mater. Phys.* 2004, 70, 214402.
- (62) Tokunaga, Y.; Homma, Y.; Kambe, S.; Aoki, D.; Sakai, H.; Yamamoto, E.; Nakamura, A.; Shiokawa, Y.; Walstedt, R. E.; Yasuoka, H. NMR Evidence for Triple-q Multipole Structure in  $\text{NpO}_2$ . *Phys. Rev. Lett.* 2005, 94, 137209.
- (63) Wen, X.-D.; Martin, R. L.; Scuseria, G. E.; Rudin, S. P.; Batista, E. R. A Screened Hybrid DFT Study of Actinide Oxides, Nitrides, and Carbides. *J. Phys. Chem. C* 2013, 117, 13122–13128.
- (64) Prodan, I. D.; Scuseria, G. E.; Martin, R. L. Assessment of Metageneralized Gradient Approximation and Screened Coulomb Hybrid Density Functionals on Bulk Actinide Oxides. *Phys. Rev. B: Condens. Matter Mater. Phys.* 2006, 73, 045104.
- (65) Andersson, D. A.; Lezama, J.; Uberuaga, B. P.; Deo, C.; Conradson, S. D. Cooperativity among Defect Sites in  $\text{AO}_{2+x}$  and  $\text{A}_4\text{O}_9$  (A=U,Np,Pu): Density Functional Calculations. *Phys. Rev. B: Condens. Matter Mater. Phys.* 2009, 79, 024110.
- (66) Gryaznov, D.; Heifets, E.; Sedmidubsky, D. Density Functional Theory Calculations on Magnetic Properties of Actinide Compounds. *Phys. Chem. Chem. Phys.* 2010, 12, 12273–12278.
- (67) Yang, Y.; Wang, B.; Zhang, P. Electronic and Mechanical Properties of Ordered (Pu,U) $\text{O}_2$  Compounds: A Density Functional Theory +U Study. *J. Nucl. Mater.* 2013, 433, 345–350.
- (68) Zhang, P.; Wang, B.-T.; Zhao, X.-G. Ground-State Properties and High-Pressure Behavior of Plutonium Dioxide: Density Functional Theory Calculations. *Phys. Rev. B: Condens. Matter Mater. Phys.* 2010, 82, 144110.
- (69) Gryaznov, D.; Rashkeev, S.; Kotomin, E. A.; Heifets, E.; Zhukovskii, Y. Helium Behavior in Oxide Nuclear Fuels: First Principles Modeling. *Nucl. Instrum. Methods Phys. Res., Sect. B* 2010, 268, 3090–3094.
- (70) Prodan, I. D.; Scuseria, G. E.; Sordo, J. A.; Kudin, K. N.; Martin, R. L. Lattice Defects and Magnetic Ordering in Plutonium Oxides: A Hybrid Density-Functional-Theory Study of Strongly Correlated Materials. *J. Chem. Phys.* 2005, 123, 014703.
- (71) Jomard, G.; Amadon, B.; Bottin, F.; Torrent, M. Structural, Thermodynamic, and Electronic Properties of Plutonium Oxides from First Principles. *Phys. Rev. B: Condens. Matter Mater. Phys.* 2008, 78, 075125.
- (72) Wen, X.-D.; Martin, R. L.; Henderson, T. M.; Scuseria, G. E. Density Functional Theory Studies of the Electronic Structure of Solid State Actinide Oxides. *Chem. Rev.* 2012, 113, 1063–1096.
- (73) Wang, H.; Konashi, K. LDA+U Study of Pu and  $\text{PuO}_2$  on Ground State with Spin-Orbital Coupling. *J. Alloys Compd.* 2012, 533, 53–57.
- (74) Steiner, S.; Khmelevskiy, S.; Marsmann, M.; Kresse, G. Calculation of the Magnetic Anisotropy with Projected-Augmented-



(75) Bo, T.; Lan, J.-H.; Wang, C.-Z.; Zhao, Y.-L.; He, C.-H.; Zhang, Y.-J.; Chai, Z.-F.; Shi, W.-Q. First-Principles Study of Water Reaction and H<sub>2</sub> Formation on UO<sub>2</sub> (111) and (110) Single Crystal Surfaces. *J. Phys. Chem. C* 2014, 118, 21935–21944.

(76) Bo, T.; Lan, J.-H.; Zhao, Y.-L.; Zhang, Y.-J.; He, C.-H.; Chai, Z.-F.; Shi, W.-Q. First-Principles Study of Water Adsorption and Dissociation on the UO<sub>2</sub> (111), (110) and (100) Surfaces. *J. Nucl. Mater.* 2014, 454, 446–454.

(77) Anisimov, V. I. *Strong Coulomb Correlations in Electronic Structure Calculations*; CRC Press, 2000.

(78) Monkhorst, H. J.; Pack, J. D. Special Points for Brillouin-Zone Integrations. *Phys. Rev. B: Solid State* 1976, 13, 5188.

(79) Blöchl, P. E.; Jepsen, O.; Andersen, O. K. Improved Tetrahedron Method for Brillouin-Zone Integrations. *Phys. Rev. B: Condens. Matter Mater. Phys.* 1994, 49, 16223.

(80) Bousquet, E.; Spaldin, N. J-dependence in the LSDA+U Treatment of Noncollinear Magnets. *Phys. Rev. B: Condens. Matter Mater. Phys.* 2010, 82, 220402.

(81) Suzuki, M.-T.; Magnani, N.; Oppeneer, P. M. Microscopic Theory of the Insulating Electronic Ground States of the Actinide Dioxides AnO<sub>2</sub> (An = U, Np, Pu, Am, and Cm). *Phys. Rev. B: Condens. Matter Mater. Phys.* 2013, 88, 195146.

(82) Csonka, G. I.; Perdew, J. P.; Ruzsinszky, A.; Philipson, P. H. T.;

Lebegue, S.; Paier, J.; Vydrov, O. A.; Angyan, J. G. Assessing the Performance of Recent Density Functionals for Bulk Solids. *Phys. Rev. B: Condens. Matter Mater. Phys.* 2009, 79, 155107.

(83) Palmer, D. C. Visualization and Analysis of Crystal Structures using CrystalMaker Software. *Z. für Kristallogr. Cryst. Mater.* 2015, 230, 559–572.

(84) Momma, K.; Izumi, F. VESTA 3 for Three-Dimensional Visualization of Crystal, Volumetric and Morphology Data. *J. Appl. Crystallogr.* 2011, 44, 1272–1276.

(85) Ganose, A. M.; Jackson, A. J.; Scanlon, D. O. SUMO: Command-line Tools for Plotting and Analysis of Periodic Ab Initio Calculations.

*Energy (eV)* 2018, 2, 0.

(86) Watson, G. W.; Kelsey, E. T.; de Leeuw, N. H.; Harris, D. J.; Parker, S. C. Atomistic Simulation of Dislocations, Surfaces and Interfaces in MgO. *J. Chem. Soc., Faraday Trans.* 1996, 92, 433–438.

(87) Sun, W.; Ceder, G. Efficient Creation and Convergence of Surface Slabs. *Surf. Sci.* 2013, 617, 53–59.

(88) Muggelberg, C.; Castell, M. R.; Briggs, G. A. D.; Goddard, D. T. An STM Study of the UO<sub>2</sub> (001) Surface. *Appl. Surf. Sci.* 1999, 142, 124–128.

(89) Tasker, P. W. The Structure and Properties of Fluorite Crystal Surfaces. *J. Phys. Colloq.* 1980, 41, C6-488–C6-491.

(90) Tasker, P. W. The Stability of Ionic Crystal Surfaces. *J. Phys. C: Solid State Phys.* 1979, 12, 4977.

(91) Tan, A. H. H.; Abramowski, M.; Grimes, R. W.; Owens, S. Surface Defect Configurations on the (100) Dipolar Surface of UO<sub>2</sub>. *Phys. Rev. B: Condens. Matter Mater. Phys.* 2005, 72, 035457.

(92) Vanpoucke, D. E. P.; Brocks, G. Formation of Pt-Induced Ge Atomic Nanowires on Pt/Ge(001): A Density Functional Theory Study. *Phys. Rev. B: Condens. Matter Mater. Phys.* 2008, 77, 241308.

(93) Vanpoucke, D. E. P.; Brocks, G. Density Functional Theory Study of Pt-Induced Ge (001) Reconstructions. *Phys. Rev. B: Condens. Matter Mater. Phys.* 2010, 81, 035333.

(94) Tersoff, J.; Hamann, D. R. Theory of the Scanning Tunneling Microscope. *Phys. Rev. B: Condens. Matter Mater. Phys.* 1985, 31, 805–813.

(95) Tafreshi, S. S.; Roldan, A.; de Leeuw, N. H. Hydrazine Network on Cu (111) Surface: A Density Functional Theory Approach. *Surf. Sci.* 2015, 637–638, 140–148.

(96) Irrera, S.; Roldan, A.; Portalone, G.; De Leeuw, N. H. The Role of Hydrogen Bonding and Proton Transfer in the Formation of Uracil Networks on the Gold (100) Surface: A Density Functional Theory Approach. *J. Phys. Chem. C* 2013, 117, 3949–3957.

(97) Santos-Carballal, D.; Roldan, A.; Grau-Crespo, R.; de Leeuw, N. H. A DFT Study of the Structures, Stabilities and Redox Behaviour of the Major Surfaces of Magnetite Fe<sub>3</sub>O<sub>4</sub>. *Phys. Chem. Chem. Phys.* 2014, 16, 21082–21097.

(98) Shields, A. E.; Santos-Carballal, D.; de Leeuw, N. H. A Density Functional Theory Study of Uranium-Doped Thoria and Uranium Adatoms on the Major Surfaces of Thorium Dioxide. *J. Nucl. Mater.* 2016, 473, 99–111.

(99) Tian, X.-f.; Wang, H.; Xiao, H.-x.; Gao, T. Adsorption of Water on UO<sub>2</sub> (111) Surface: Density Functional Theory Calculations.

*Comput. Mater. Sci.* 2014, 91, 364–371.

(100) Taylor, T. N.; Ellis, W. P. Distorted Surface Oxygen Structure on UO<sub>2</sub>(100). *Surf. Sci.* 1981, 107, 249–262.

(101) Broqvist, P.; Kullgren, J.; Wolf, M. J.; van Duin, A. C. T.; Hermansson, K. ReaxFF Force-Field for Ceria Bulk, Surfaces, and Nanoparticles. *J. Phys. Chem. C* 2015, 119, 13598–13609.

(102) Hodkin, E. N.; Nicholas, M. G. Surface and Interfacial Properties of Non-Stoichiometric Uranium Dioxide. *J. Nucl. Mater.* 1977, 67, 171–180.

(103) Hodkin, E. N.; Nicholas, M. G. Comments on “Surface, Grain Boundary and Interfacial Energies in UO<sub>2</sub> and UO<sub>2</sub>-Ni” by P. Nikolopoulos et al. *J. Nucl. Mater.* 1978, 74, 178.

(104) Hodkin, E. N.; Nicholas, M. G. Surface and Interfacial Properties of Stoichiometric Uranium Dioxide. *J. Nucl. Mater.* 1973, 47, 23–30.

(105) Ellis, W. P. Low-Energy Electron Diffraction Studies of Uranium Dioxide. *J. Chem. Phys.* 1968, 48, 5695–5701.

(106) Muggelberg, C.; Castell, M. R.; Briggs, G. A. D.; Goddard, D. T. The Atomic Structure of the UO<sub>2</sub> (111) Surface and the Effects of Additional Surface Oxygen Studied by Elevated Temperature STM. *Surf. Rev. Lett.* 1998, 05, 315–320.

(107) Castell, M. R.; Dudarev, S. L.; Muggelberg, C.; Sutton, A. P.; Briggs, G. A. D.; Goddard, D. T. Surface Structure and Bonding in the Strongly Correlated Metal Oxides NiO and UO<sub>2</sub>. *J. Vac. Sci. Technol., A* 1998, 16, 1055–1058.

(108) Castell, M. R. Wulff Shape of Microscopic Voids in UO<sub>2</sub> Crystals. *Phys. Rev. B: Condens. Matter Mater. Phys.* 2003, 68, 235411.

(109) Boyarchenkov, A. S.; Potashnikov, S. I.; Nekrasov, K. A.; Kupryazhkin, A. Y. Molecular Dynamics Simulation of UO<sub>2</sub> Nano-crystals Surface. *J. Nucl. Mater.* 2012, 421, 1–8.

(110) Bottin, F.; Geneste, G.; Jomard, G. Thermodynamic Stability of the UO<sub>2</sub> Surfaces: Interplay between Over-Stoichiometry and Polarity Compensation. *Phys. Rev. B* 2016, 93, 115438.

(111) Abramowski, M.; Grimes, R. W.; Owens, S. Morphology of UO<sub>2</sub>. *J. Nucl. Mater.* 1999, 275, 12–18.

(112) Nikolopoulos, P.; Nazare, S.; Thümmel, F. Surface, Grain Boundary and Interfacial Energies in UO<sub>2</sub> and UO<sub>2</sub>-Ni. *J. Nucl. Mater.* 1977, 71, 89–94.